Biophysical Journal, Volume *120*

Supplemental information

Local rigidification and possible coacervation of the *Escherichia coli* DNA by cationic nylon-3 polymers

Yanyu Zhu, Lei Liu, Mainak Mustafi, Leslie A. Rank, Samuel H. Gellman, and James C. Weisshaar

Table S1. Characterization of nylon-3 polymers.

Polymer	$Đ_{GPC}$[a]	Mn_{GPC}[b]	Dp_{NMR}[c]	M_{NMR}[d]
MM-CH	1.070	7841	32	3954
MM homopolymer	1.167	2038	22	2693
DM-DMCP	1.08	6538	13	1879
DM-DMCH	1.08	3235	14	2041

[a] Polymer length dispersity = *Mw/Mn.*

[b] The number-averaged molecular weight of side-chain protected polymers determined from GPC.

[c] The degree of polymerization, or average polymer chain length, as calculated by NMR integrations based on end group analysis, i.e., the assumption that each chain contains only one *tert*-butyl benzoyl group.

[d] Average molecular weight of side-chain deprotected polymers calculated based on NMR. The polymers are in the form of trifluoroacetate salts. The polymers are used in the form of aqueous solution, so the molecular weight of trifluoroacetate counter anions are not included.

Table S2. Bacterial strains

Strain	Species imaged	Strain details	Background strain	Expression method
JCW154	*Right2-parS* by ParB-GFP	Ref. (1)	MG1655	Plasmid
JCW10	Periplasmic GFP	Ref. (2)	MG1655	Plasmid
MDG196	Ribosome S2-mEos2	Ref. (3)	VH1000	Chromosome
MSG192	Ribosome S2-YFP	Ref. (4,5)	VH1000	Chromosome
MG1655	WT	—	MG1655	—
VH1000	WT	—	VH1000	—
SM7	HU-PAmCherry	Ref. (5)	VH1000	Plasmid
Dendra2	Ribosome S2-Dendra2	Ref. (6)	MG1655	Chromosome

Explanation of Videos

Video S1

Corresponding to data in Fig. 1. Effects of copolymer MM-CH on a representative *E. coli* cell that exports GFP to the periplasm. Phase contrast image (left), fluorescence snapshots of GFP (middle) and Sytox Orange (right) are shown. Flow of 2× MIC of MM-CH in EZRDM with 5 nM of the DNA stain Sytox Orange begins at $t = 0$. Images were acquired at 12 s per frame for 90 min.

Video S2

Corresponding to data in Fig. 3E. Phase contrast inage (left), Sytox Orange fluorescence (middle) and ribosome S2-YFP fluorescence (right) snapshots of single *E. coli* cell at different times during the attack of copolymer MM-CH are shown. Cells with ribosomal S2 subunit labeled with YFP were stained with 500 nM Sytox Orange for 10 min before imaging. 2× MIC MM-CH flowed beginning at $t = 0$. Images were acquired at 1 min per frame for 90 min.

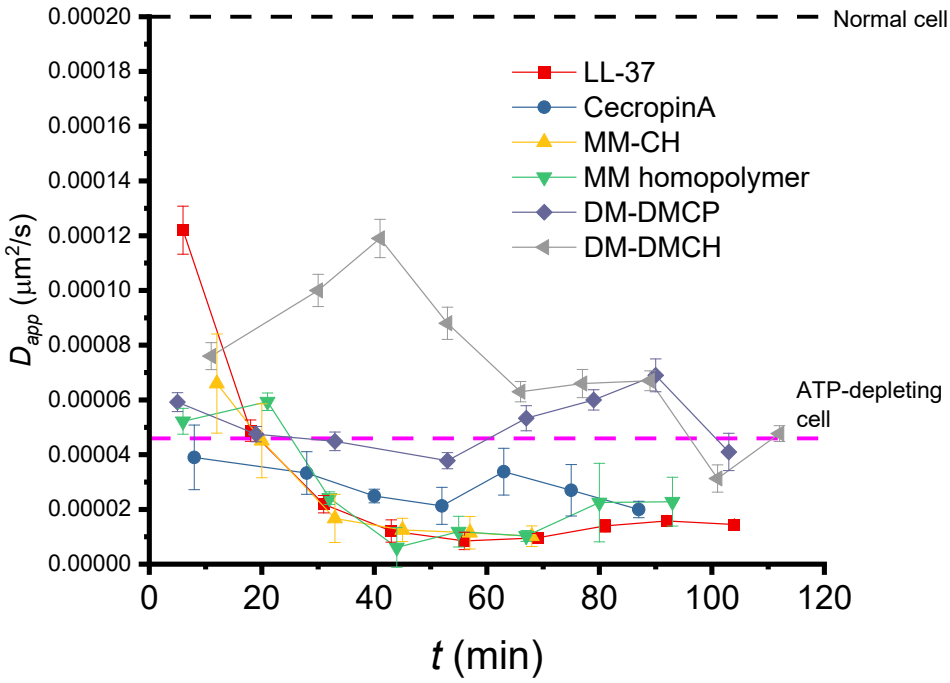

Figure S1. Apparent diffusion coefficient of DNA loci as a function of time after the onset of treatment with AMP or polymer at $t = 0$. Each time point represents the average over a 10-min window with images taken at 1s/frame. The time plotted for each point is the center of the 10-min window. The apparent diffusion coefficient D is obtained from a linear fit to the first 10 points in the MSD plot. Reference value for normal cells and ATP depleted cells are shown as the black dashed line and purple dashed line.

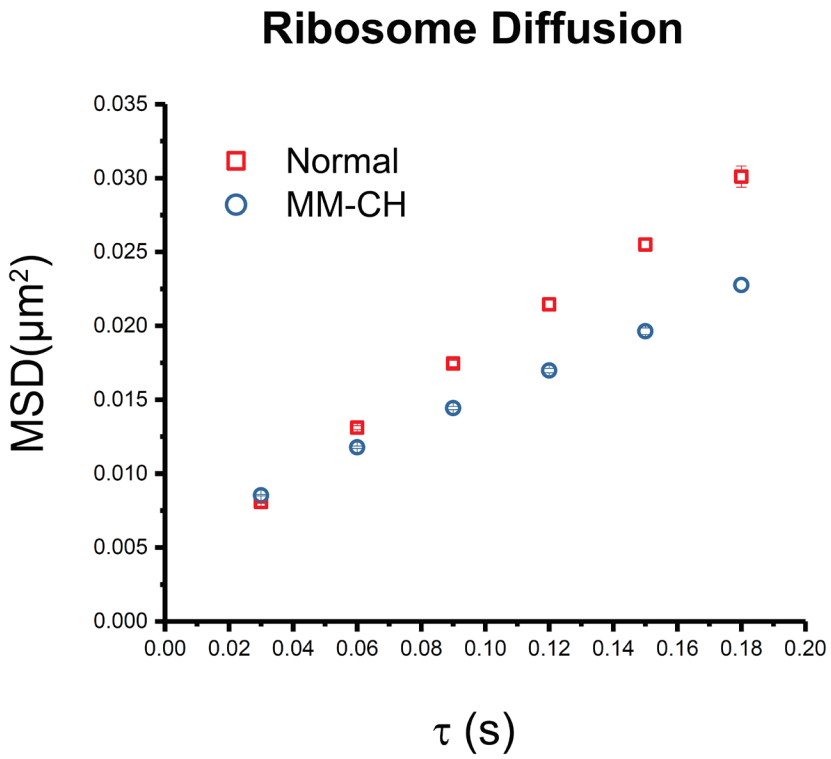

Figure S2. Ribosomal species MSD vs lag time from S2-Dendra2 trajectories taken at 30 ms/frame in two different conditions as shown. The apparent diffusion coefficient D_{app} is obtained by linear fitting of the first three data points. The numerical results are: (0.039 ± 0.002) $\mu m^2/s$ for normal growth; (0.025 ± 0.001) $\mu m^2/s$ for cells 25 min after onset of MM-CH treatment.

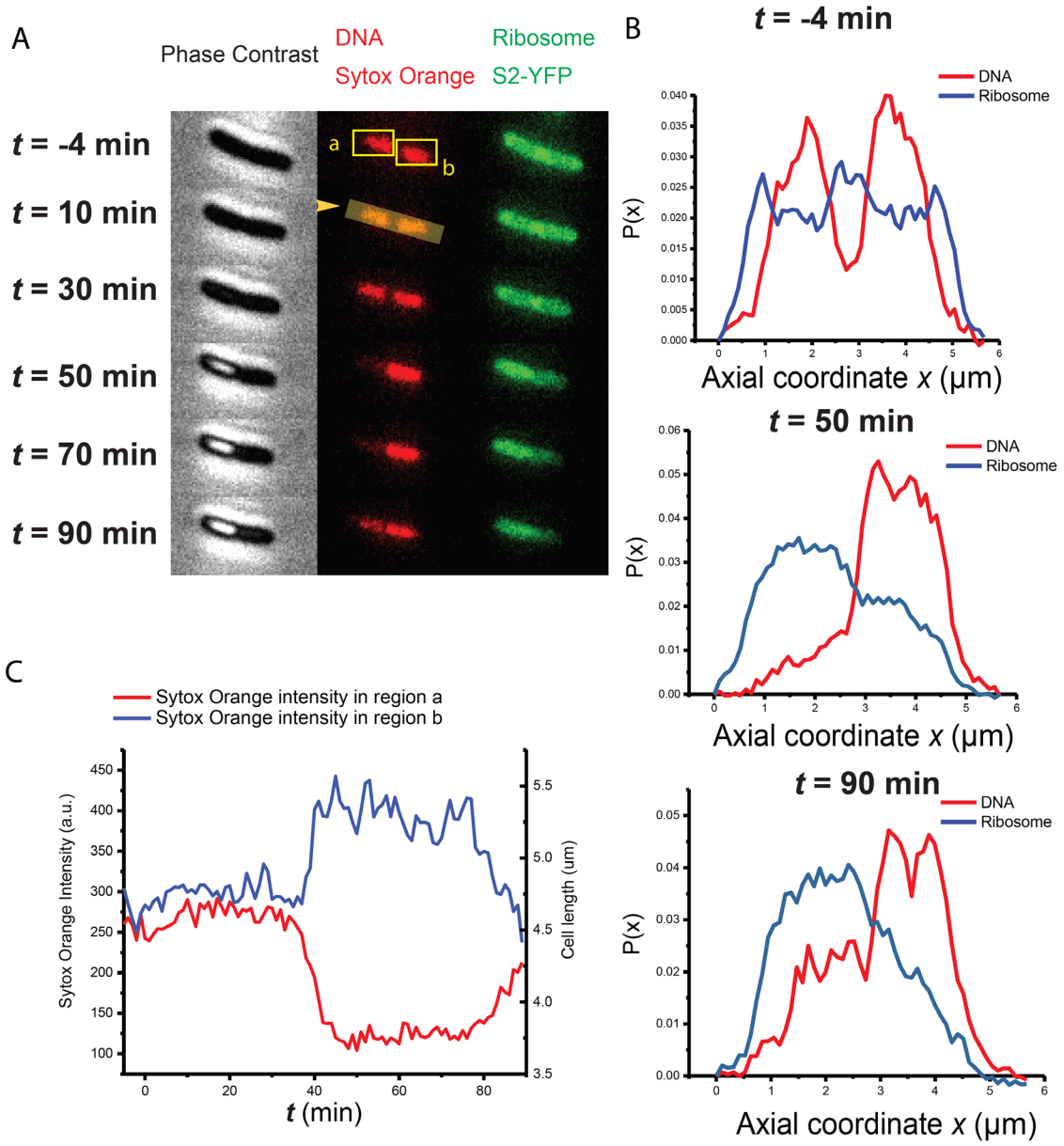

Figure S3. Ribosome-DNA segregation throughout large-scale nucleoid morphology changes. Cells with ribosome S2 subunit labeled with YFP were stained with 500 nM Sytox Orange for 10 min before imaging. 2× MIC MM-CH flowed beginning at $t = 0$. Images were acquired at 1 min per frame. (A) Phase contrast, Sytox Orange fluorescence and ribosome S2-YFP snapshots of single *E. coli* cell at different times. (B) For the same cell shown in (A), projected axial Sytox Orange and YFP projected axial intensity profiles (direction of arrowhead in panel (A)). (C) Sytox Orange intensity vs time for the same cell shown in panel (A). Sytox Orange intensity in the left nucleoid lobe (red curve, region a in panel (A)), and in the right nucleoid lobe (blue curve, region b in panel (A)) are shown separately.

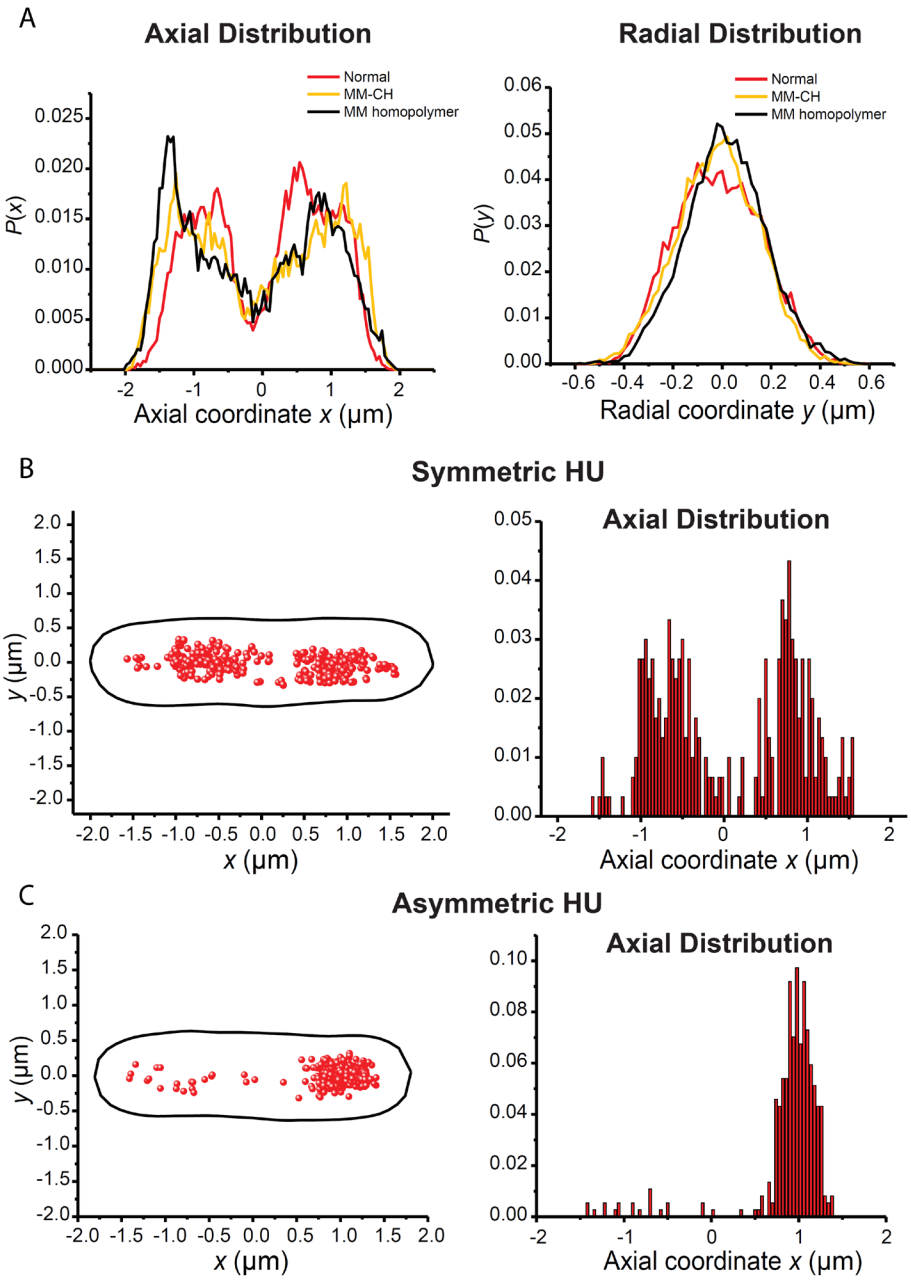

Figure S4. HU-PAmCherry super-resolution spatial distribution imaged in normal cells and after treatment with polymer. (A) Cell-averaged HU spatial distribution in cells with length of 4.0–4.3 μm. Projected axial (*left*) and radial (*right*) distribution of HU in normal cells and 25 min after the onset of MM-CH copolymer and MM homopolymer treatment. Radial distribution includes only molecules in the nucleoid region (0.4 μm < $|x|$ < 1.2 μm). (B,C) Two examples of single-cell DNA (HU-PAmCherry) spatial distributions exhibiting after MM-CH treatment. The cell in panel B shows two symmetric axial lobes, whereas the cell in panel C shows asymmetric lobes. *Left*: scatter plot of HU locations. Black line is cell mesh generated from phase contrast image using Oufti program. *Right*: axial distribution of HU locations.

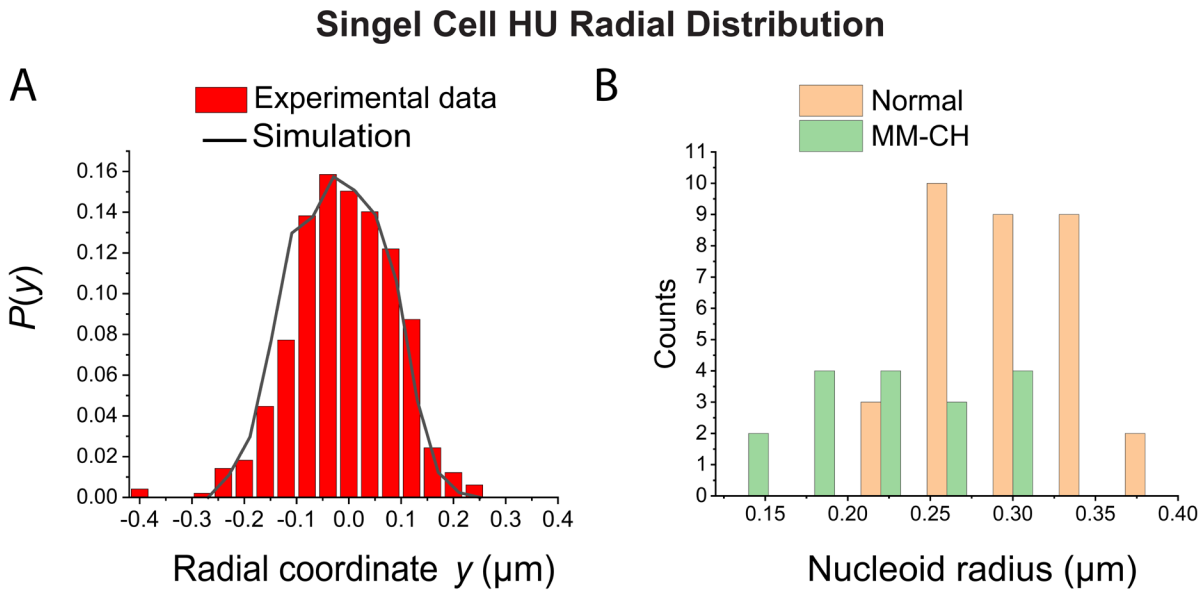

Figure S5. Quantitative determination of nucleoid radius in normal cells and after treatment with MM-CH. (A) Single cell HU radial distributions (red) of an example cell with cell length 4.1 μm. Black lines: simulated radial projections of particles uniformly distributed within a spherocylinder of radius r = 0.16 μm. (B) Distribution of single-cell nucleoid radii for cells in normal growth condition and 25 min after 2X MIC MM-CH with two nucleoid lobes. Only cells in the length range of 4.0-4.3 μm are included. For each cell, the radius was determined by fitting the HU nucleoid radial distributions with calculated projections from a uniform distribution within a spherocylinder. Radius was varied to find the best fit.

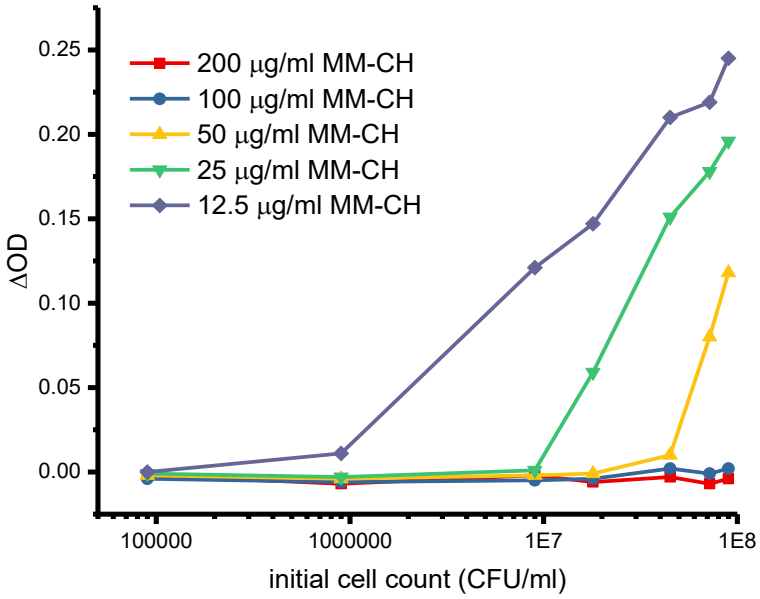

Figure S6. Determination of the MM-CH initial concentration required to kill a given concentration of bacterial cells. For each MM-CH concentration and for each initial cell count, we measured the optical density (OD) at 595 nm before and after 24-hour incubation of the cells with MM-CH. The change in OD is defined as $\Delta OD = OD_{t=24h} - OD_{t=0}$. For a given MM-CH concentration, as the CFU/ml increases, ΔOD becomes significantly greater than zero when the initial number of cells becomes too large to be completely killed by the MM-CH concentration provided.

GPC and NMR characterization of nylon-3 polymers

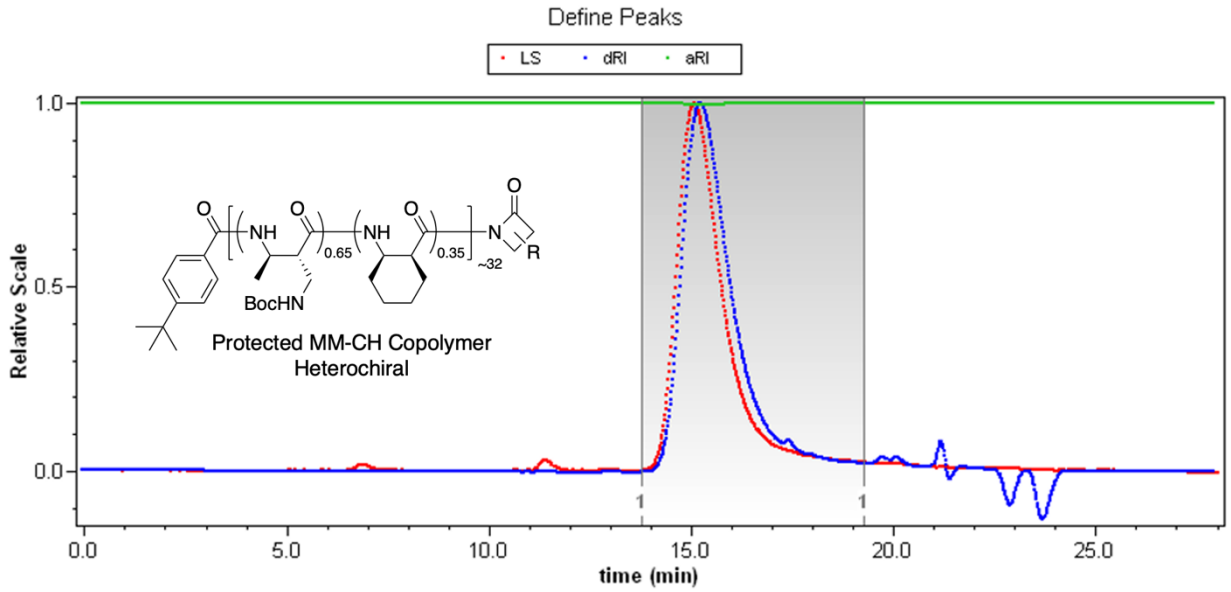

Figure S7. GPC chromatogram of MM-CH (Boc protected amine) copolymer, with the mobile phase of THF at 40˚C. Red line represents detection via light scattering (LS), and blue line represents detection via differential refractive index (dRI). The LS peak eluting from 6 to 8 minutes is attributed to a large molecule weight polymer from the column stationary phase.

Polymer	$Đ_{GPC}$	Mn
MM-CH	1.07	7841

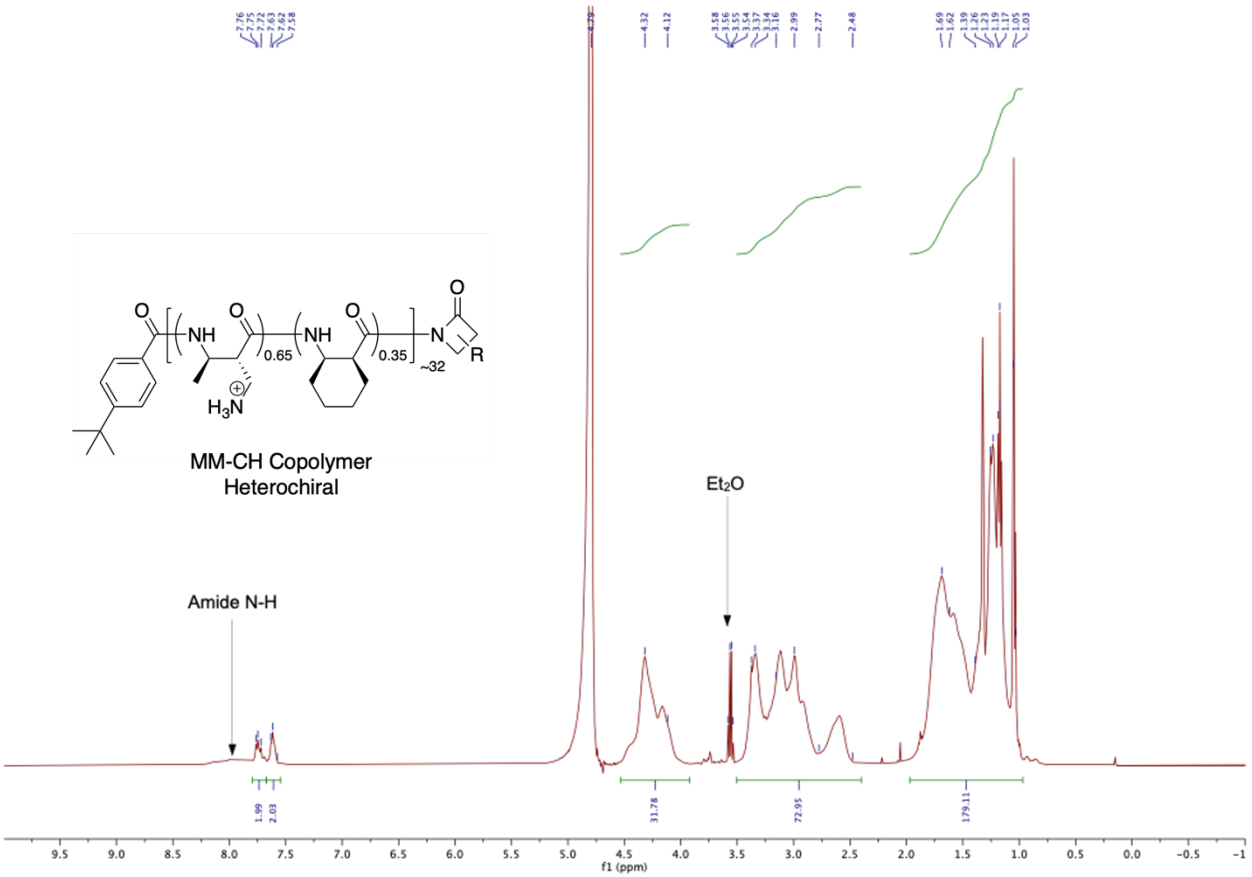

Figure S8. ^{1}H NMR spectrum (500 MHz, D_2O) of MM-CH deprotected copolymers.

Calculations for Dp_{NMR} and subunit ratio of MM-CH copolymer:

31.78 = 1 MM proton + 1 CH proton

72.95 = 3 MM protons+1 CH proton

179.11 = 3 MM protons + 8 CH protons + 9 Initiator protons

MM ≈ 20.6 and CH ≈ 11.2

DP_{NMR} = MM + CH ≈ 32

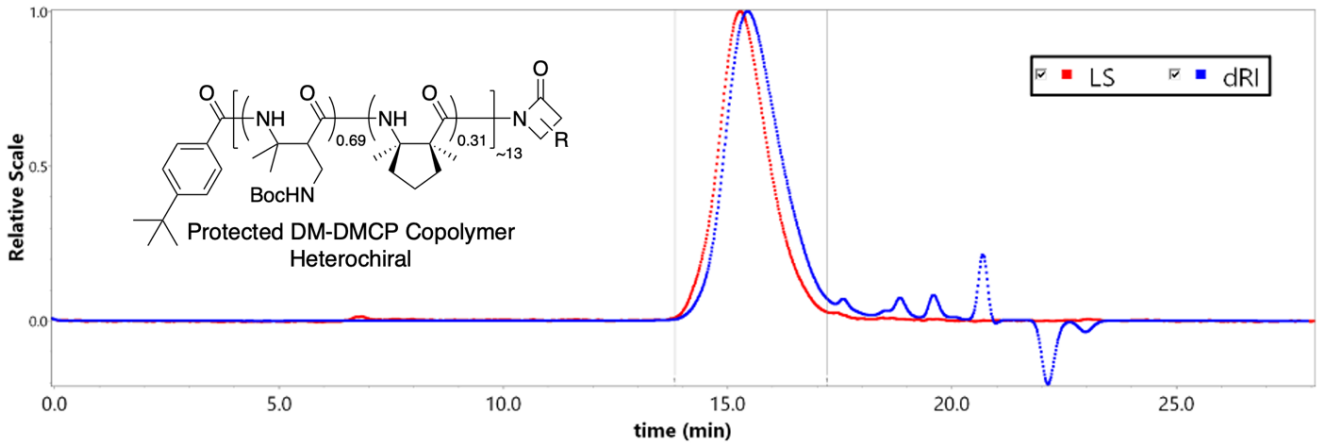

Figure S9. GPC chromatogram of DM-DMCP (Boc protected amine) copolymer, with the mobile phase of THF at 40˚C. Red line represents detection via light scattering (LS), and blue line represents detection via differential refractive index (dRI). The LS peak eluting from 6 to 8 minutes is attributed to a large molecule weight polymer from the column stationary phase.

Polymer	$Đ_{GPC}$	Mn
DM-DMCP	1.08	6538

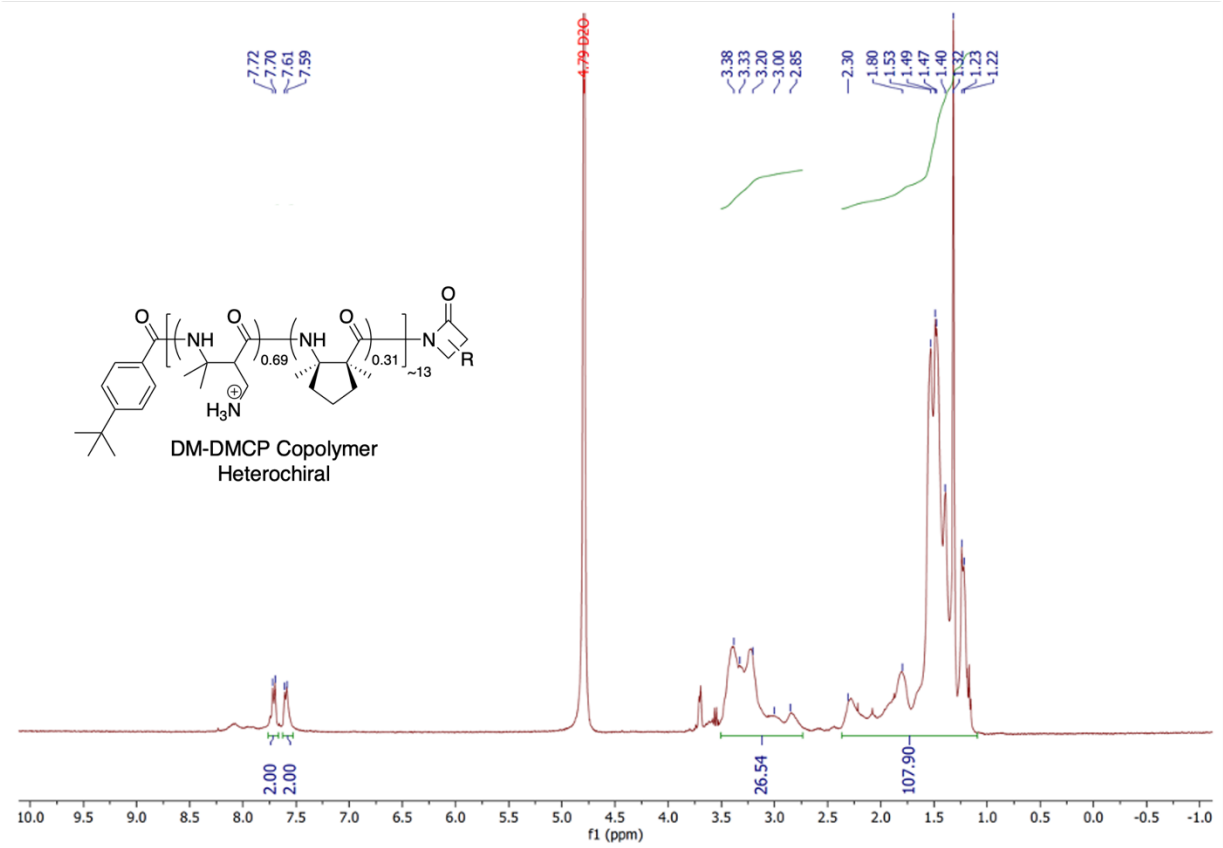

Figure S10. ^{1}H NMR spectrum (500 MHz, D_2O) of DM-DMCP deprotected copolymers.

Calculations for Dp_{NMR} and subunit ratio of DM-DMCP copolymer:

26.54 = 3 DM protons

107.90 = 6 DM protons + 12 DMCP protons + 9 Initiator protons

DM≈9 and DMCP ≈ 4

DP_{NMR} = DM + DMCP = 13

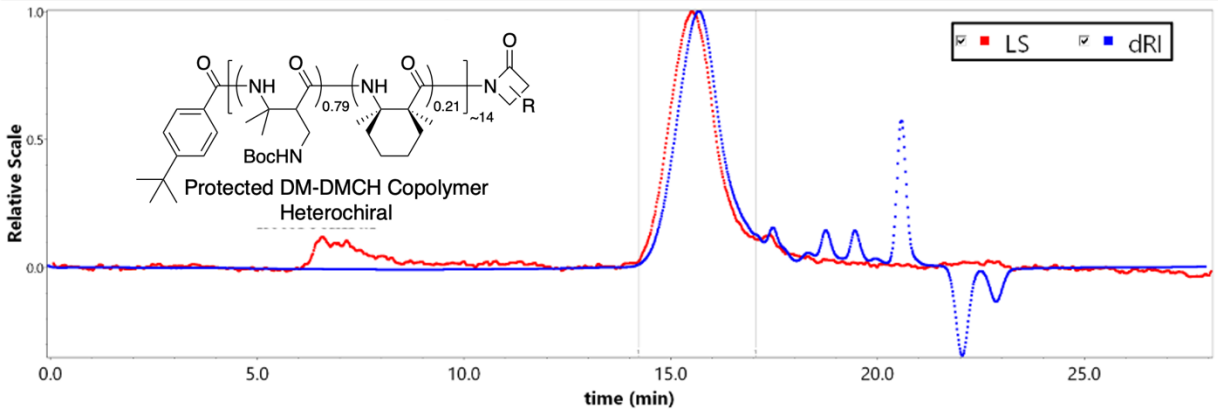

Figure S11. GPC chromatogram of DM-DMCH (Boc protected amine) copolymer, mobile phase THF, 40˚C. Red line represents detection via light scattering (LS), and blue line represents detection via differential refractive index (dRI). The LS peak eluting from 6 to 8 minutes is attributed to a large molecule weight polymer shed from the column stationary phase.

Polymer	$Đ_{GPC}$	Mn
DM-DMCH	1.08	3235

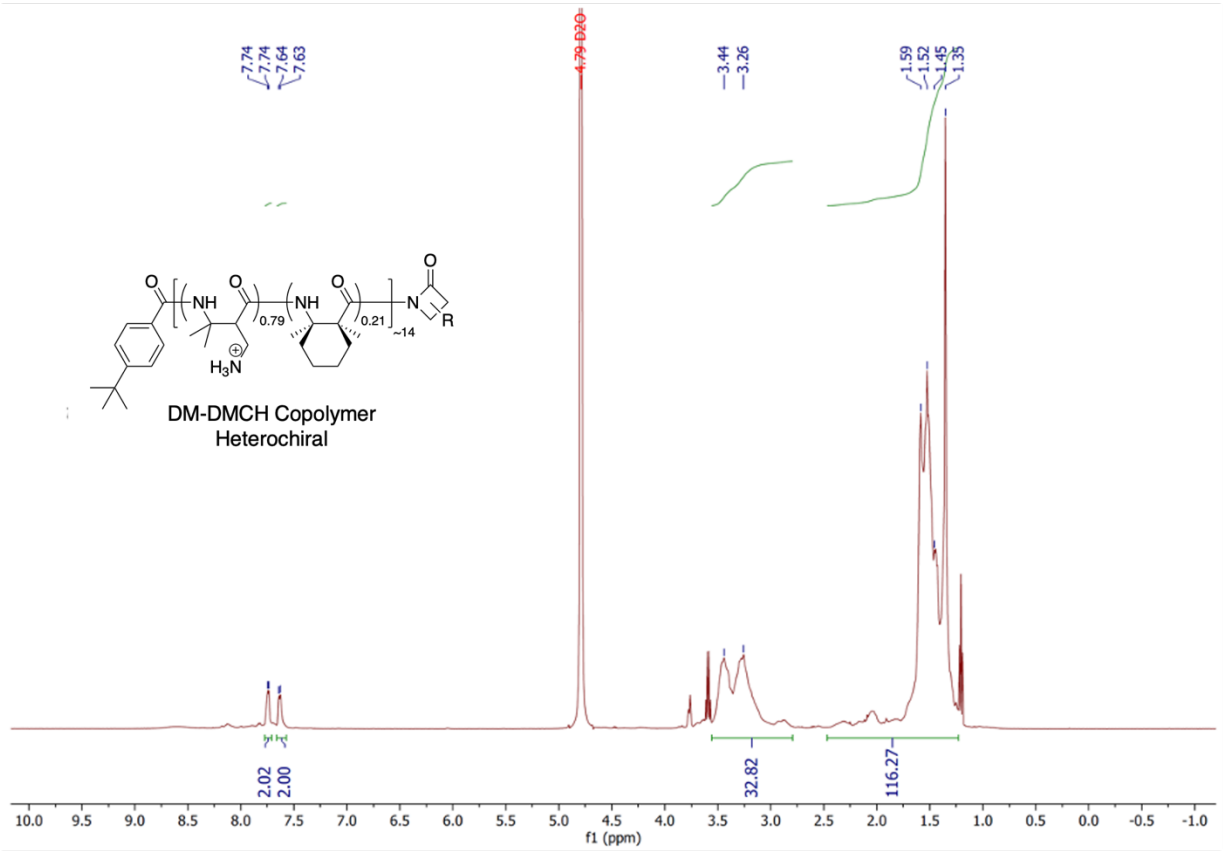

Figure S12. ^{1}H NMR spectrum (500 MHz, D_2O) of DM-DMCH deprotected copolymers.

Calulations for Dp_{NMR} and subunit ratio of DM-DMCH copolymer:

32.82 = 3 DM protons

116.27 = 6 DM protons + 14 DMCH protons + 9 Initiator protons

DM≈11 and DMCH ≈ 3

DP_{NMR} = DM + DMCH = 14

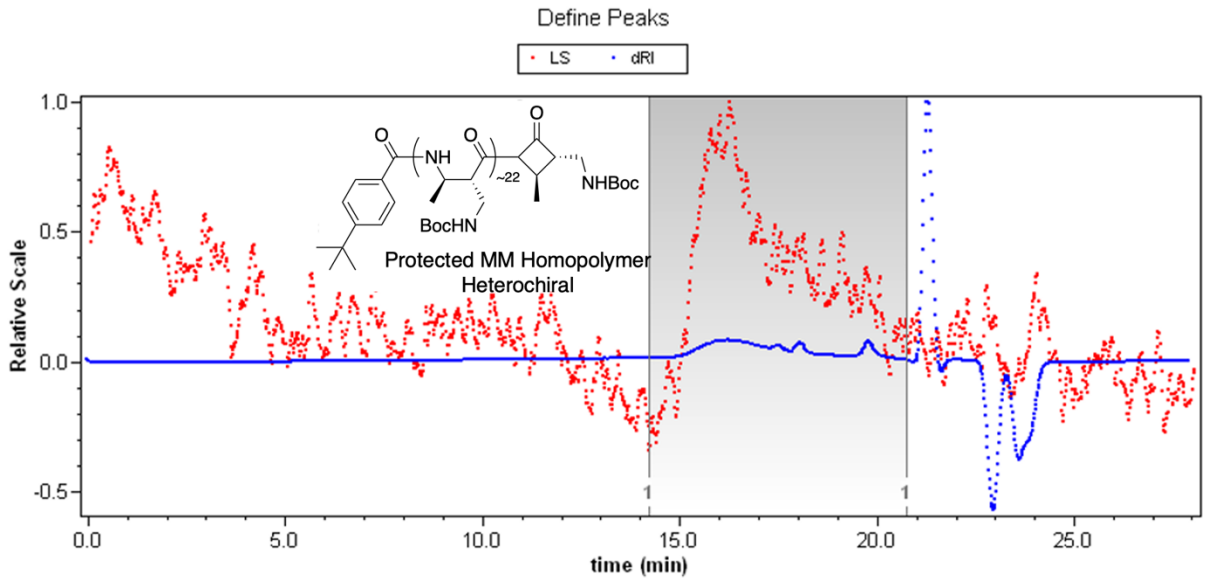

Figure S13. GPC chromatogram of MM (Boc protected amine) homopolymer, mobile phase THF, 40˚C. Red line represents detection via light scattering (LS), and blue line represents detection via differential refractive index (dRI).

Polymer	$Đ_{GPC}$	Mn
MM Homopolymer	1.17	2038

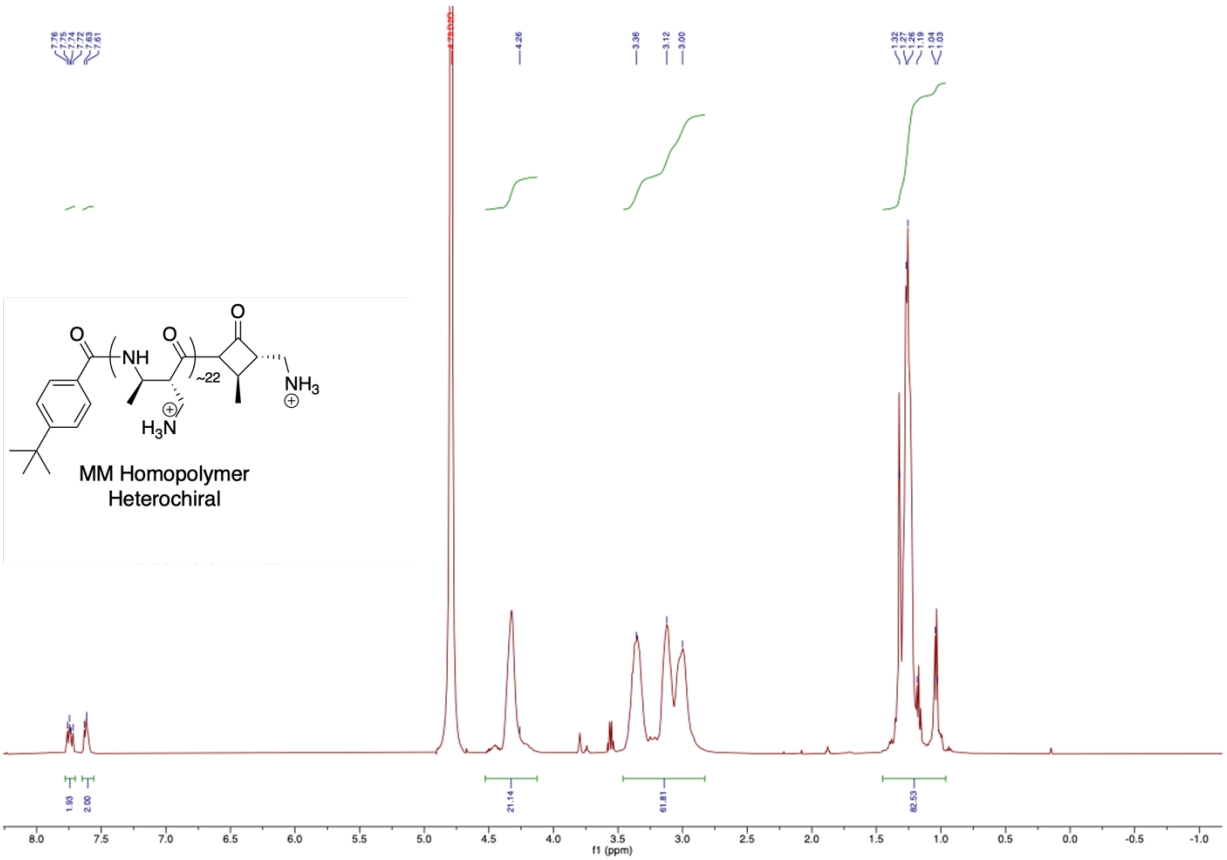

Figure S14. ^{1}H NMR spectrum (500 MHz, D_2O) of deprotected MM homopolymer.

<u>Calulations for Dp_{NMR} and subunit ratio of MM homopolymer:</u>

21.14 = 1 MM proton

61.81 = 3 MM protons

82.53 = 3 MM protons + 9 Initiator protons

MM≈22

DP_{NMR} = 22

Synthesis of Nylon-3 polymers

The β-lactam solution in tetrahydrofuran (THF) was added a solution of the co-initiator precursor, p-tert-butylbenzoyl chloride in THF (7). The amount of the co-initiator depended on the intended degree of polymerization. For instance, for an average chain length of 20, 0.05 equivalents of the co-initiator precursor relative to the total quantity of β-lactam monomers was used in the polymerization reaction. Then a solution of lithium bis(trimethylsilyl)amide in THF (2.5 equivalents of this base relative to the amount of p-tert-butylbenzoyl chloride) was added, and the mixture was stirred overnight at room temperature. A few drops of methanol were added to the reaction to quench the polymerization reactions. Then polymers were isolated by precipitation with pentanes. Copolymers at the protected stage (with Boc groups on the side chain nitrogens) were analyzed by gel permeation chromatography (GPC) using THF as the mobile phase. Side chain groups of polymers were deprotected using neat trifluoroacetic acid (TFA) with 5% (v/v) of triisopropylsilane (TIPS) relative to TFA. The deprotected copolymers were characterized by proton nuclear magnetic resonance (^{1}H NMR) spectroscopy.

Proton (^{1}H) Nuclear Magnetic Resonance (NMR) spectra for all polymers were obtained on a Bruker Avance III spectrometer at 500 MHz. All proton chemical shifts are reported in ppm using the solvent as the internal standard (D_2O at 4.790 ppm). Gel permeation chromatography (GPC) analysis, with THF as eluent, involved two involved two Waters columns (Styragel HR 4E and HR 2 particle size 5 μm) linked in series. The Waters liquid chromatography unit (Alliance) was equipped with a multiangle light scattering detector (Wyatt miniDAWN TREOS, 658 nm) and a refractive index detector (Wyatt Optilab-rEX, 658 nm). The number average molecular weight (*Mn*) and dispersity (*Đ*) of polymers included in Table S1 were calculated using ASTRA software with a d*n*/d*c* value of 0.1 mL/g.

Cell growth and preparation for imaging

Bulk cultures were grown in EZ rich, defined medium (EZRDM), which is a morpholinepropanesulfonic acid (MOPS)-buffered solution at pH = 7.4 supplemented with metal ions (M2130; Teknova), glucose (2 mg/mL), amino acids and vitamins (M2104; Teknova), nitrogenous bases (M2103; Teknova), 1.32 mM K_2HPO_4, and 76 mM NaCl. Cultures were grown from glycerol frozen stock to stationary phase overnight at 30°C. Subcultures were grown to exponential phase (OD = 0.2–0.6 at 600 nm) at 30°C before sampling for the microscopy experiments.

Strains used in the study and the corresponding MIC are summarized in Tables 1, S1, and S2. Strains that express labeled species from a plasmid are grown with addition of 100 μg/mL ampicillin. When the cells reach mid-log phase, anhydrotetracycline was added to a final concentration of 45 nM to induce the expression of the labeled protein of interest. After 10 min of induction, the cells were centrifuged and resuspended in fresh growth media with 100 μg/mL ampicillin to remove the inducer. The cells were then incubated again in growth media for 15 min at 30°C to enable maturation of the labeled protein of interest prior to imaging. For studying cells under ATP-depleting conditions, cells were treated with 200 μM carbonylcyanide-*m*-chlorophenylhydrazone (CCCP) plus 1 mM 2-deoxyglucose (8-13). These were added to the subcultures for 10 min prior to imaging. During the imaging, EZRDM was supplemented with each drug at the same concentration.

Two different imaging methodologies were employed, a flow chamber and a static chamber. Single-cell, time-lapse imaging experiments on the ribosome S2-YFP, ppGFP, nucleoid stained by Sytox Orange (S11368, Thermo-Fisher Scientific) and DNA locus *Right2* were carried out at 30°C in a PDMS-based microfluidics chamber consisting of a single rectilinear channel of uniform height of 50 μm, width of 6 mm and length of 11 mm. The total

chamber volume is ~10 μL. After attachment of the PDMS chamber to the glass coverslip, 10 μL of 0.01% poly-L-lysine (molecular weight >150,000 Da) was flowed through the chamber and allowed to adsorb for 30 min. The chamber was then rinsed thoroughly with ultrapure water to remove excess poly-L-lysine. When the subcultures had grown to midlog phase, we flowed culture containing *E. coli* cells through the microfluidic chamber, followed by fresh, aerated, warmed EZRDM to wash away any unbound cells. The remaining cells are immobilized on the coverslip but grow normally. The PDMS ceiling of the microfluidics device is permeable to the ambient gases N_2 and O_2. The microfluidics chamber allows flowing of appropriate chemicals necessary for the experiment such as polymer solution or Sytox Orange during imaging.

Single-molecule imaging of ribosomes S2-mEos2, ribosome S2-Dendra2 and HU-PAmCherry was carried out in a static chamber. First, ~150 μL of cell culture was placed within a CoverWell perfusion chamber gasket (Invitrogen) on a poly-L-lysine -coated, cleaned coverslip to fill the entire chamber volume. We allowed 2 min for the cells to adhere to the coverslip. The plated cells were then rinsed with the appropriate fresh, warmed, aerated media to wash away any non-adhered cells. For imaging of cells under normal growth conditions, the rinsing medium is EZRDM. Cells continue to grow normally for at least 30 min under these conditions. For AMP or polymer treated conditions, the rinsing medium is AMP or polymer in EZRDM solution. The cells are grown in the corresponding medium and maintained at 30°C throughout the imaging using an automatic temperature controller.

For nucleoid staining experiments, Sytox Orange dye was added to a growing mid-log-phase culture (OD = 0.2–0.6 at 600 nm) to a final concentration of 500 nM (14). After 10 min of incubation, the cells were centrifuged twice and resuspended in fresh EZRDM before imaging. The rinsing steps eliminate background fluorescence from dye molecules that adhere to the coverslip without removing Sytox Orange from the cytoplasm.

Microscopy

All imaging was performed on a Nikon Eclipse Ti inverted microscope (Nikon) with an oil immersion 100×, 1.45 N.A. phase contrast objective (CFI Plan Apo Lambda DM; Nikon Instrument). The images were further magnified 1.5×. Fast shutters (Uniblitz LS2; Vincent Associates) were used to synchronize illumination and image acquisition. Images were recorded by a back-illuminated EMCCD camera with 16 μm × 16 μm pixels (either Andor iXon DV-897 or Andor iXon DV-887; Andor Technology). Each pixel corresponds to 105 × 105 nm^2 at the sample with an overall magnification of 150×.

Studies of the motion of the DNA loci *Right2* labeled by ParB-GFP (strain JCW154) were imaged using 488 nm excitation (Coherent Sapphire laser), expanded to illuminate the field of view uniformly. The laser intensity was ~100 W/cm^2 at the sample plane. The emission filter was HQ525/50 (Chroma Technology). The labeled ParB-GFP protein polymerizes specifically at a *parS* site engineered into the chromosome near the locus *Right 2*, forming bright puncta. The loci could be tracked with good signal-to-noise for 600 camera frames at 1s/frame and 50 ms exposure time.

For experiments with dual color imaging of ppGFP (green channel) and Sytox Orange (red channel), μManager was used to obtain the data and switch filters between frames using a LB10-NW filter wheel (Sutter). The time-lapse videos were obtained as 50 ms exposure time each, with green fluorescence (488 nm excitation), red fluorescence (561 nm excitation), and phase contrast images interleaved (12 s per complete cycle). To minimize spectral bleed-through in the two-color experiments, we utilized the narrower filters HQ510/20 for the green channel and HQ600/50M for the red channel. Laser intensities at the sample were typically ~5 W/cm^2 at 488 nm and ~2.5 W/cm^2 at 561 nm. For dual color experiments imaging ribosome S2-YFP

(green channel) and Sytox Orange (red channel), the same microscopic parameters were applied except 1 min per imaging cycle.

For super-resolution imaging of HU-PAmCherry (strain SM7), ribosomes labeled by S2-mEos2 (strain MDG196) and S2-Dendra2, the fluorescent protein was photoconverted using a 405 nm laser at ~ 4-12 W/cm^2 and subsequently imaged using a 561 nm excitation laser at ~2 kW/cm^2. The emission filter was ET610/75 (Chroma Technology). HU-PAmCherry, ribosome S2-mEos2 and ribosome S2-Dendra2 were imaged at a frame rate of 31.2 Hz, with an exposure time of 30 ms.

Minimum Inhibitory Concentration (MIC) Assay

The MIC value for the AMPs and polymers were determined using the broth microdilution method as previously described (8). Two-fold serial dilutions of drug in 1× EZRDM were performed in separate rows of a polystyrene 96-well plate, with each plate containing an inoculum of *E. coli*. The inoculum was a 1:20 dilution from a bulk culture at midlog phase (OD600 = 0.5) grown at 30°C. The plate was incubated at 30°C and shaken at 200 rpm in a Lab-Line Orbital Environ Shaker (Model 3527) for 6 hr. The MIC value was taken as the lowest concentration for which no growth was discernible (<0.05 OD) after 6 hr.

Data analysis

Images were analyzed using a MATLAB graphical user interface (GUI) developed in our lab (15). Images were smoothed and filtered to obtain a zero-based image. Bright spots were located with pixel-level accuracy by a peak finding algorithm that detects the local intensity maxima within an image. A user defined intensity threshold was used as the minimum brightness of a pixel arising from a single molecule. The threshold is carefully set by the user so that it will not be so high as to reject a real single molecule in the raw images or so low as to include background noise.

A modified MATLAB version of the tracking program written by Crocker and Grier (16) was used. As before (4), a centroid algorithm was used to locate the identified particles with subpixel resolution. Centroids of the bright spots were calculated from a 7 x 7 pixel square containing the entire bright spot, centered on the local maximum determined by the peak finding algorithm. The centroid positions from successive frames were connected to form a trajectory. In each experimental condition, the ensemble-averaged mean-square displacement was calculated as:

$$MSD(\tau) = \langle\left(\vec{R}(t+\tau) - \vec{R}(t)\right)^2\rangle = \frac{1}{N}\sum_i \frac{1}{m}\sum_m [\vec{R}_i(mt+\tau) - \vec{R}_i(mt)]^2$$

Here N is the number of trajectories over which the ensemble average is taken. The index m runs from 1 to a specific value given the lag time τ, providing the time average of each trajectory. The final MSD is an average over the ensemble and over time. For DNA loci imaged with 1 s/frame time, m runs from 1 to 99. We used the linear fit of the first 10 points on the MSD plots to calculate an approximate apparent diffusion coefficient. For ribosomal S2-mEos2, ribosomal S2-Dendra2 and HU-PAmCherry, m runs from 1 to 6 and we used the linear fit of the first 3 points on the MSD plots to calculate an approximate apparent diffusion coefficient via an average over thousands of trajectories (17).

Suppose the least-squares, best fit to the first 10 or 3 experimental points of a mean-square displacement plot is given by the equation $\mathrm{MSD}(\tau) = a + b\tau$, with b the slope and a the extrapolated intercept at lag time $\tau = 0$. Then Michalet (17) has shown that the most accurate mean diffusion coefficient is given by $D = b/4$ and the best estimate of the dynamic localization error is $\sigma = \frac{1}{2}\,(a + 4Dt_E/3)^{1/2}$, where t_E is the exposure time per camera frame. Mean diffusion coefficients of different species in the various experiment of conditions are collected in Tables 4.

In the HU super-resolution distribution section, to obtain the tip-to-tip cell length and to define the (x,y) coordinates of each particle within the cell, cell outlines were generated from

phase contrast images by the open-source image analysis software Oufti (18). To generate the spatial distribution of HU molecules, the camera based coordinates are reoriented so that the *x* axis and *y* axis correspond to the long and short principle cell axes.

Continued segregation of DNA and ribosomes after MM-CH treatment

In normally growing *E. coli* cells, the DNA and the ribosomal species are strongly segregated from each other. Ribosome-DNA exclusion plays an important role in shaping DNA morphology (19,20). To explore the spatial distributions of DNA and ribosomes after MM-CH treatment, we stained the DNA of bacteria strain MSG192 (Table S2) with Sytox Orange as above. In this strain, the ribosomal S2 protein is labeled with YFP. S2 resides on the surface of the 30S ribosomal subunit. As before, we flowed 2× MIC MM-CH beginning at $t = 0$. Images of phase contrast, Sytox Orange, and ribosome S2-YFP were interleaved at an overall cycle time of 1 min per frame. A representative bacterial cell is shown in Fig. S3A and Video S2. As before (19,20), in normal growth conditions prior to the addition of MM-CH, ribosomes are concentrated axially in the endcaps and at the cell center and radially in the thin annular region surrounding each nucleoid lobe. DNA remains in the nucleoid region and shows two axial peaks. There is a strong anticorrelation between the spatial distributions of DNA and the ribosomes (Fig. S3A, B).

At $t \sim 40$ min, the left nucleoid lobe has largely merged with the right lobe (Fig. S3A-C). At the same time, much of the ribosome distribution has moved to the left side of the cell, where the DNA has become sparse. The strong anticorrelation of DNA and ribosome distributions persists. Interestingly, the phase contrast image shows a white band that grows in where the ribosomes accumulate but DNA is depleted. This is a region of relatively low refractive index. Even at $t = 90$ min, when the left nucleoid lobe has partially recovered, the ribosomes still preferentially locate in the left side of the cell. Evidently the right nucleoid lobe remains dense

enough to exclude the ribosomes even at a very late stage. Out of 23 observed cells, 16 showed DNA and ribosome morphological changes similar to those described above.

Upper Bound on Amount of charge on MM-CH absorbed per cell

The method to quantify the absorbed MM-CH is based on that described previously by the Wimley lab (21). We applied this method to determine the amount of MM-CH and charges absorbed per cell for the lowest concentration of MM-CH that kills all the cells in the sample.

We first prepared combinations of different concentrations of MM-CH and different initial cell counts to determine the number of MM-CH molecules needed to kill the bacteria at different cell counts. We grew cells to OD = 1.0 or higher in EZRDM, then centrifuged and resuspended the cells in 1× PBS. After that we determine the CFU in each sample by measurement of OD600 and the scaling equation OD 1.0 = 1.5×10^8 CFU/mL. Serial dilution using 1× PBS then provided a range of initial cell counts. We incubated each specific number of cells with various specific concentrations of MM-CH in the test tube in PBS solution for 60 min at 30°C. After that we added 50 µL solution from each tube (each particular combination of cell number and MM-CH concentration) to polystyrene 96-well plates supplemented with 50 µL 2× EZRDM in each well. We measured the OD595 ($OD_{t=0}$), incubated 24 h, and measured the OD 595 again ($OD_{t=24\ h}$). Thus, we could determine the 24 h OD increase ($\Delta OD = OD_{t=24\ h} - OD_{t=0}$) for each particular combination (Fig. S6). If the OD does not increase significantly after 24 h, then the initial MM-CH concentration was sufficient to kill that initial number of cells. In this way we can set the minimum bulk MM-CH concentration which is required to kill a particular initial number of cells.

For example, we found 25 µg/mL MM-CH can completely kill bacteria with initial count of 9×10^6 CFU/mL, but not a higher initial count. The ratio of total MM-CH copies to the initial number of cells provides an upper bound on the number of copies absorbed per cell. The

combination of 25 μg/mL MM-CH and 9×10^6 CFU/mL yields an upper bound of ~2.8×10^{-6} μg MM-CH absorbed per cell. Since there is a distribution of polymer chain length, we cannot directly calculate number of polymers per bacterial cell. However, the ratio of cationic subunit MM and hydrophobic subunit CH is fixed, in our case MM: CH = 64.8 % : 35.2%.

Suppose A = MM subunit, with charge +1 , molecular weight M_A = 228.7 g/mol and mol fraction of A = n_A =64.8%; Suppose B = CH subunit, with charge 0, molecular weight M_B= 125.17 g/mol and mol fraction of B = n_B = 35.2%; The degree of polymerization N = 32 determined by NMR. We can calculate

$$\text{weight faction of A : } w_A = \frac{M_A \times n_A}{M_A \times n_A + M_B \times n_B} = 77.8\%$$

$$\text{weight faction of B : } w_B = \frac{M_B \times n_B}{M_A \times n_A + M_B \times n_B} = 22.2\%$$

And the number of total charges in 1 mL solution is :

$$\frac{25\ \mu g/mL \times 77.8\% \times 1mL}{228.17\ g/mol} = 5.13 \times 10^{16}$$

Then number of total charges per cell is:

$$\frac{25\ \mu g/mL \times 77.8\%}{228.17\ g/mol \times 9 \times 10\text{^}6\ CFU/mL} = 5.7 \times 10^9$$

Similar calculation can be applied for MM-CH concentration of 50 μg/mL, whose critical initial cell concentration occurred at 4×10^7 CFU/ml. The number of charges per cell is ~2.6×10^9. Of course, the conditions in these MM-CH uptake experiments are quite different from those in the microscopy experiments. The uptake experiments are carried out in PBS to avoid interference in the absorption measurements by the multitude of species present in EZRDM. In addition, in the microscopy experiments the flow of a constant concentration of MM-CH provides an unlimited source of peptide after membrane permeabilization has occurred. And not all the MM-CH enters the cell and the cytoplasm. Nevertheless, we view ~10^9 positive charge absorbed per cell as a sensible first estimate. The average degree of polymerization determined

by NMR is N =32; The polydispersity Mw/Mn is1.07 determined from GPC (Table S1), and this indicates a narrow chain length distribution. Therefore, most of charges are on the polymer longer than 30 units.

Under our growth conditions the ~2.3 chromosomes carry ~2.1 x 10^7 negative phosphate charges, compensated by cytoplasmic counterions such as K^+ (22). The ~50,000 ribosomes, each with charge of –4500, bring a total of ~2.2×10^8 negative charges (4). Half of these charges are compensated by ribosomal proteins and structural Mg^{2+} cations (22). The ~375,000 tRNA copies carry ~80 phosphates each for a total of ~3×10^7 negative charges (23). The mRNA contributes more or less the same as tRNA (24). These cytoplasmic species alone provide ~2×10^8 negative charges (~ 200 mM) residing in cytoplasmic polyanionic species that are compensated primarily by K^+.

Spatial distribution of DNA revealed by super-resolution imaging of HU

To confirm the results obtained from single-cell, widefield imaging, we study the DNA distribution by super-resolution microscopy using a strain SM7, which expresses HU- PAmCherry from a plasmid after induction. HU dimer is a nucleoid-associated protein that binds nonspecifically to the chromosomal DNA. We have shown before that the distribution of HU is a good proxy for the chromosomal DNA distribution, as judged by its comparison with Sytox Orange (20). The images were taken at 30 ms per frame.

We first obtained the composite distribution of HU averaged across cells in a narrow cell length range of 4–4.3 μm determined from the tip-to-tip length in phase contrast images. We projected this distribution onto the cell long axis to form the axial 1D distributions *P(x)* and onto the cell short axis to form the radial distribution *P(y)* (Fig. S4A). Radial distribution includes only molecules in the nucleoid region (0.4 μm < $|x|$ < 1.2 μm). The composite distribution averaged across different cells look similar for normal cells and cells after the polymer treatment (Fig. S4A). However, there is more heterogeneity

among the cells after polymer and results in a more irregular composite axial distribution. The overall HU radial distribution is also slightly narrower for cells after polymer.

The heterogeneity is more obvious when we look at the single cell HU distribution. We found cells after MM-CH which have enough detected HU molecules per cell to exhibit a clear pattern can be classified into two categories. The first type of cells has the usual symmetric distribution of HU, as shown in Fig. S4B. The other category has an asymmetric distribution of HU, i.e. HU was distributed mostly at one end of the cell. It could either be the case where all the HU molecules are in one side of the cell or the case where there are molecules on both sides, but one side has too few molecules so that the axial peak ratio is greater than 5:1 (Fig. S4C).

For cells after MM-CH in the length range of 4–4.3 μm, we have 17 cells showing symmetric distribution of HU; 22 cells showing asymmetric distribution of HU. For cells after MM-CH in the length range of 3.5–4 μm, we have 46 cells exhibiting symmetric distribution of HU; 43 cells showing asymmetric distribution of HU. In contrast, for cells in normal growth condition in the length range of 4–4.3 μm, there is 52 cells showing normal symmetric two-lobe distribution while only 2 cells exhibiting asymmetric distribution. Therefore, the large fraction of cells with asymmetric HU after MM-CH is not caused by random probability but due to the effect of MM-CH.

We next compared the single cell nucleoid radius of cells without treatment and cells 25 min after MM-CH and with two nucleoid lobes. We determined the single cell nucleoid radius by fitting the HU radial distribution $P(y)$ to a simulated distribution for a uniformly filled spherocylinder with various radius to find the best fit. The nucleoid radius distribution are shown in Fig S5.

Supporting References

1. Espeli, O., R. Mercier, and F. Boccard. 2008. DNA dynamics vary according to macrodomain topography in the *E. coli* chromosome. *Mol. Microbiol.* 68(6):1418-1427, doi: 10.1111/j.1365-2958.2008.06239.x.
2. Sochacki, K. A., I. A. Shkel, M. T. Record, and J. C. Weisshaar. 2011. Protein Diffusion in the Periplasm of *E. coli* under Osmotic Stress. *Biophys. J.* 100(1):22-31.
3. Bakshi, S., H. Choi, J. Mondal, and J. C. Weisshaar. 2014. Time-dependent effects of transcription- and translation-halting drugs on the spatial distributions of the *Escherichia coli* chromosome and ribosomes. *Mol. Microbiol.* 94(4):871-887, doi: 10.1111/mmi.12805.
4. Bakshi, S., A. Siryaporn, M. Goulian, and J. C. Weisshaar. 2012. Superresolution imaging of ribosomes and RNA polymerase in live *Escherichia coli* cells. *Mol. Microbiol.* 85(1):21-38, doi: 10.1111/j.1365-2958.2012.08081.x.
5. Mohapatra, S., and J. C. Weisshaar. 2018. Functional mapping of the *E. coli* translational machinery using single-molecule tracking. *Mol. Microbiol.* 110:262-282, doi: 10.1111/mmi.14103.
6. English, B. P., V. Hauryliuk, A. Sanamrad, S. Tankov, N. H. Dekker, and J. Elf. 2011. Single-molecule investigations of the stringent response machinery in living bacterial cells. *Proc. Natl. Acad. Sci. U.S.A.* 108(31):E365-E373.
7. Mowery, B. P., A. H. Lindner, B. Weisblum, S. S. Stahl, and S. H. Gellman. 2009. Structure-activity Relationships among Random Nylon-3 Copolymers That Mimic Antibacterial Host-Defense Peptides. *J. Am. Chem. Soc.* 131(28):9735-9745.
8. Choi, H., Z. Yang, and J. C. Weisshaar. 2015. Single-cell, real-time detection of oxidative stress induced in *Escherichia coli* by the antimicrobial peptide CM15. *Proc. Natl. Acad. Sci. U. S. A.* 112(3):E303-310, doi: 10.1073/pnas.1417703112.
9. Stannard, J. N., and B. L. Horecker. 1947. The *In vitro* Inhibition of Cytochrome Oxidase by Azide and Cyanide. *Fed. Proc.* 6(1):210-210.
10. Weber, S. C., A. J. Spakowitz, and J. A. Theriot. 2012. Nonthermal ATP-dependent fluctuations contribute to the in vivo motion of chromosomal loci. *Proc. Natl. Acad. Sci. U. S. A.* 109(19):7338-7343, doi: 10.1073/pnas.1119505109.
11. Cavari, B. Z., Y. Avidor, and Grossowi.N. 1967. Effect of Carbonyl Cyanide M-Chlorophenylhydrazone on Respiration and Respiration-Dependent Phosphorylation in *Escherichia coli*. *Biochem. J.* 103(2):601-&.
12. Weber, S. C., A. J. Spakowitz, and J. A. Theriot. 2010. Bacterial chromosomal loci move subdiffusively through a viscoelastic cytoplasm. *Phys. Rev. Lett.* 104(23):238102, doi: 10.1103/PhysRevLett.104.238102.
13. Kralj, J. M., D. R. Hochbaum, A. D. Douglass, and A. E. Cohen. 2011. Electrical Spiking in *Escherichia coli* Probed with a Fluorescent Voltage-Indicating Protein. *Science*. 333(6040):345-348.
14. Bakshi, S., H. Choi, N. Rangarajan, K. J. Barns, B. P. Bratton, and J. C. Weisshaar. 2014. Nonperturbative imaging of nucleoid morphology in live bacterial cells during an antimicrobial peptide attack. *Appl. Environ. Microbiol.* 80(16):4977-4986, doi: 10.1128/AEM.00989-14.

15. Bakshi, S., B. P. Bratton, and J. C. Weisshaar. 2011. Subdiffraction-limit study of Kaede diffusion and spatial distribution in live *Escherichia coli*. *Biophys. J.* 101(10):2535-2544, doi: 10.1016/j.bpj.2011.10.013.
16. Crocker, J. C., and D. G. Grier. 1996. Methods of Digital Video Microscopy for Colloidal Studies. *J. Colloid Interface Sci.* 179(1):298-310, doi: https://doi.org/10.1006/jcis.1996.0217.
17. Michalet, X. 2010. Mean square displacement analysis of single-particle trajectories with localization error: Brownian motion in an isotropic medium. *Phys. Rev. E Stat. Nonlin. Soft Matter Phys.* 82(4 Pt 1):041914, doi: 10.1103/PhysRevE.82.041914.
18. Paintdakhi, A., B. Parry, M. Campos, I. Irnov, J. Elf, I. Surovtsev, and C. Jacobs-Wagner. 2016. Oufti: an integrated software package for high-accuracy, high-throughput quantitative microscopy analysis. *Mol. Microbiol.* 99(4):767-777.
19. Bakshi, S., H. Choi, and J. C. Weisshaar. 2015. The spatial biology of transcription and translation in rapidly growing *Escherichia coli*. *Front. Microbiol.* 6:636, doi: 10.3389/fmicb.2015.00636.
20. Mohapatra, S., and J. C. Weisshaar. 2018. Functional mapping of the *E. coli* translational machinery using single-molecule tracking. *Mol. Microbiol.*, doi: 10.1111/mmi.14103.
21. Starr, C. G., J. He, and W. C. Wimley. 2016. Host Cell Interactions Are a Significant Barrier to the Clinical Utility of Peptide Antibiotics. *ACS Chem. Biol.* 11(12):3391-3399, doi: 10.1021/acschembio.6b00843.
22. Record, M. T., Jr., E. S. Courtenay, D. S. Cayley, and H. J. Guttman. 1998. Responses of *E. coli* to osmotic stress: large changes in amounts of cytoplasmic solutes and water. *Trends Biochem. Sci.* 23(4):143-148.
23. Dong, H., L. Nilsson, and C. G. Kurland. 1996. Co-variation of tRNA abundance and codon usage in *Escherichia coli* at different growth rates. *J. Mol. Biol.* 260(5):649-663, doi: 10.1006/jmbi.1996.0428.
24. Joyeux, M. 2016. In vivo compaction dynamics of bacterial DNA: A fingerprint of DNA/RNA demixing? *Current Opinion in Colloid & Interface Science*. 26:17-27.